

## Analytical and Numerical Modeling of R Curves for Cracks with Bridging Zones

John A. Nairn

Received: 13 June 2008 / Accepted: 16 March 2009

**Abstract** At the onset of fracture in materials with process zones, the fracture resistance, or  $R$  curve, rises as the process zone develops. After process zone development, crack propagation proceeds by steady state growth. By considering  $J$  integral contours inside and outside the process zone, the available energy can be partitioned into crack tip energy release rate and process zone energy. To model the rising  $R$  curve, however, required assumptions about damage mechanisms in the process zone and partitioning of its energy into released and recoverable energy. By considering process zones that are elastic fiber-bridging zones with softening regions caused by fiber breakage or damage, equations for rising  $R$  curves were derived as a function of crack tip toughness and bridging zone mechanics. The new methods were implemented into the Material Point Method for generalized numerical crack propagation simulations with bridging zones. The simulation method includes pure fracture mechanics and pure cohesive zone models as extreme special cases. The most realistic simulations for many materials will likely fall between these two extremes. The results guided comments on interpretation of experimental  $R$  curves.

**Keywords** J Integral · Process Zone · Bridging Zone · Crack Bridging · Cohesive Zone · Traction Law · Numerical Modeling

### 1 Introduction

Examples of materials that develop process zones at the crack tip during crack propagation are wood [Smith and Vasic, 2003], fibrous composites [Hashemi et al, 1990, Matsumoto and Nairn, 2007], and cementitious composites [Li et al, 1987]. A process zone results in two crack tips — the actual crack tip at the end of the zone and the notch root at its beginning (see  $x_0$  and  $x_{root}$  in Fig. 1). At the onset of fracture, the

---

John A. Nairn  
Oregon State University, Wood Science & Engineering  
112 Richardson Hall, Corvallis, OR 97330, USA  
Tel.: +1-541-737-4265  
Fax: +1-541-737-3333  
E-mail: John.Nairn@oregonstate.edu

process zone develops by crack tip propagation while the notch root remains fixed. In this phase, the observed toughness evolves as characterized by a rising  $R$  or fracture resistance curve. After the process zone is fully developed, crack propagation proceeds by steady state or self-similar crack growth involving simultaneous propagation of both the crack tip and the notch root; the process zone length remains constant (anything else would not be self-similar). In this phase, the observed toughness is constant until edge effects influence the process zone. If the fully developed process zone is sufficiently small, the fracture can be analyzed by conventional fracture mechanics [Bao and Suo, 1992]. If the process zone is larger, but still smaller than the specimen, the  $R$  curve will rise and plateau at the steady state toughness. If process zone is somewhat larger, the fracture process may never reach steady state within the specimen and the entire toughness will be a rising  $R$  curve. Fracture analysis for such materials requires modeling of rising  $R$  curves.

The starting equation for prior analyses of process zones is to apply Rice's [Rice, 1968]  $J$  integral to a contour outside the zone and account for crack-surface tractions within the zone [Bao and Suo, 1992]; the result is denoted here as  $J_{ff}$  for far-field  $J$  integral:

$$J_{ff} = J_{tip} + \int_0^{\delta_{root}} \sigma(\delta) d\delta \quad (1)$$

where  $J_{tip}$  is energy release rate for crack tip propagation and the integral is the energy associated with crack tractions in the process zone;  $\sigma(\delta)$  is the crack surface traction as a function of crack opening displacement, COD or  $\delta$ , and  $\delta_{root}$  is the COD at the notch root or  $\delta(x_{root})$ . Physically,  $J_{ff}$  is the energy release rate associated with self-similar crack growth [Rice, 1968], which implies simultaneous propagation of the crack tip and the notch root such that the process zone length remains constant [Bao and Suo, 1992]. Crack propagation in the rising portion of the  $R$  curve, however, is non-self-similar because the process zone length is changing. Thus  $J_{ff}$ , in general, is not the correct energy release rate for that portion of the  $R$  curve. This fact has usually been ignored in prior work.

During crack growth, energy is released. Here the  $R$  curve is defined as the actual amount of energy released as a function of the extent of crack propagation. When process zones are present, a typical  $R$  curve will start at some initiation value and then increase to a steady-state value. The increase is a consequence of the development of the process zone. Because Eq. 1 only applies to crack propagation during steady-state conditions, that equation is insufficient for analysis of the rising portion of the  $R$  curve. A full  $R$  curve analysis requires additional assumptions about the process zone mechanics and some new equations. This paper considers only elastic process zones, such as fiber bridging zones, that undergo damage, such as by fiber breakage, resulting in traction laws containing softening regions. By accounting for energy released by such bridging zones,  $R$  curve equations were derived. This concept was used to develop a Material Point Method (MPM) simulation of full  $R$  curves. A special case of the simulations provided a new approach to elastic cohesive zone modeling by dynamically eliminating the crack tip singularity. This paper concludes with remarks on measuring and interpreting  $R$  curves.

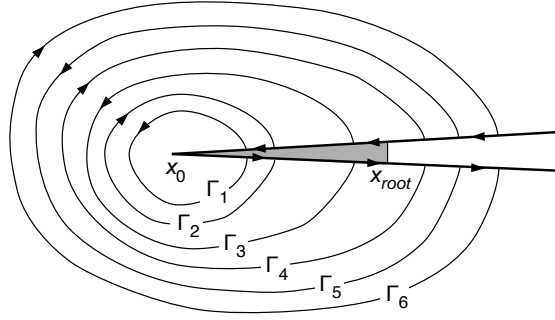


**Fig. 1** All possible combinations of  $J$  Integral paths that start and stop at the same location  $x$  when a crack has a bridging zone. The bridging zone extends from the actual crack tip at  $x_0$  to the notch root at  $x_{root}$ .

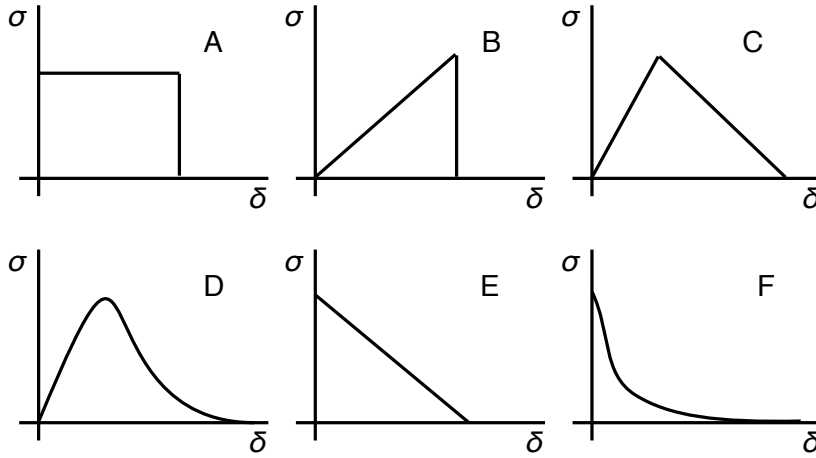


**Fig. 2** Examples of commonly assumed traction laws: A. Rigid plastic law. B. Linear elastic brittle law. C. Triangular law with initial linear elastic regime followed by a linear softening regime. D. An arbitrary traction law, often approximated with a cubic function. E. Linear softening law. F. Nonlinear softening law.

## 2 $J$ Integral Analysis of Bridging Zones

Tractions within a bridging zone in 2D fracture problems can be resolved into tractions normal and tangential to the crack surface,  $\mathbf{T}_Z = (\sigma_n(\delta), \sigma_t(\delta))$ . In bridging zone modeling, these tractions depend on the crack opening displacements normal and tangential to the crack surface,  $\delta = (\delta_n, \delta_t)$ . Figure 2 shows some generic traction laws. The traction typically increases to a peak or cohesive stress and then decreases to zero at a critical COD where the tractions fail. The term “law” in traction law is used here by convention. Although it implies these laws are a universal material property, there are no compelling experimental or theoretical justifications for that assumption.

This section considers  $J$  integral analysis of a crack having tractions from the actual crack tip at  $x_0$  to the edge of the bridging zone at  $x_{root}$  (see Fig. 1). Following Rice [1968], a  $J$  integral analysis along the path consisting of  $\Gamma_1$  in the counter-clockwise direction,  $\Gamma_2$  in the clockwise direction, and traction-loaded crack surfaces connecting

$\Gamma_1$  and  $\Gamma_2$  results in

$$J(x_1) - \int_{x_1}^{x_2} \mathbf{T}_Z \cdot \frac{d\mathbf{u}_\ell}{dx} dx - J(x_2) - \int_{x_2}^{x_1} (-\mathbf{T}_Z) \cdot \frac{d\mathbf{u}_u}{dx} (-dx) = 0 \quad (2)$$

where  $x_i$  is the  $x$  coordinate where contour  $\Gamma_i$  intersects the crack (selected to be the same on the two crack surfaces),  $\mathbf{u}_\ell$  and  $\mathbf{u}_u$  are displacements on the lower and upper crack surfaces, and

$$J(x) = \int_{\Gamma(x)} \left( W dy - \mathbf{T} \cdot \frac{d\mathbf{u}}{dx} dx \right) \quad (3)$$

is the usual  $J$  integral evaluated in the counter-clockwise direction along the path  $\Gamma(x)$  from one crack surface to the other at the location  $x$ . Here,  $W$  is strain energy,  $\mathbf{T}$  is traction, and  $\mathbf{u}$  is displacement. By definition,  $\boldsymbol{\delta} = \mathbf{u}_u - \mathbf{u}_\ell$ , resulting in

$$J(x_1) - J(x_2) + \int_{x_1}^{x_2} (\mathbf{T}_Z) \cdot \frac{d\boldsymbol{\delta}}{dx} dx = 0 \quad (4)$$

Writing the energy required to load the crack tractions to any displacement as

$$W_B(x) = \int_0^{\boldsymbol{\delta}(x)} \mathbf{T}_Z \cdot d\boldsymbol{\delta} \quad \text{with} \quad \frac{dW_B(x)}{dx} = \mathbf{T}_Z \cdot \frac{d\boldsymbol{\delta}}{dx} \quad (5)$$

it follows that

$$J(x_1) - J(x_2) + W_B(x_2) - W_B(x_1) = 0 \quad (6)$$

or, equivalently, that

$$J(x_1) - W_B(x_1) = J(x_2) - W_B(x_2) \quad (7)$$

In principle, this analysis allows for coupled tractions [Needleman, 1987]. All results in this paper, however, are for mode I cracking such that the traction energy integral simplifies to

$$W_B(x) = \int_0^{\delta(x)} \sigma(\delta) d\delta \quad (8)$$

where  $\delta(x) = \delta_n(x)$  and  $\sigma(\delta) = \sigma_n(\delta)$ .

By Eq. 7, the term

$$J_{tip} = J(x) - W_B(x) \quad x \leq x_{root} \quad (9)$$

defines a path-independent integral for all paths starting and stopping within the bridging zone. These paths are slightly less general than usual  $J$  integrals because they must start and stop at the same position  $x$ . Equation 1 from the literature refers to  $J_{ff}$  contours entirely outside the bridging zone. Thus, Eq. 9 can be viewed as extension of prior literature results to contours within the bridging zone. The equality between  $J_{tip}$  in Eq. 1 and the  $J_{tip}$  in Eq. 9 is derived by considering a contour at  $x_{root}$ , and noting that for this special case  $J_{ff} = J(x_{root})$  and  $W_B(x_{root})$  is the integral term in Eq. 1. Also note that  $J_{tip}$  is not equal to a  $J$  integral close to the crack tip or  $J(x)$ . It starts with that calculation, but then must subtract energy associated with the crack-surface tractions at the location chosen to define the contour.

Repeating this analysis for paths  $\Gamma_5$ ,  $\Gamma_6$ , and the connecting traction-free crack surfaces is identical to Rice [1968], and thus defines a second path-independent integral:

$$J_{ff} = J(x) \quad x > x_{root} \quad (10)$$

Finally, considering paths  $\Gamma_3$ ,  $\Gamma_4$ , and the partially traction-loaded crack surfaces leads to a connection between  $J_{tip}$  and  $J_{ff}$

$$J_{ff} = J_{tip} + W_B(x_{root}) \quad (11)$$

which is simply a derivation of Eq. 1 for the mode I tractions considered here [Bao and Suo, 1992].

Because a crack with a bridging zone has two tips, it is essential to have two  $J$  integrals. Physically,  $J_{ff}$  is the energy release rate for simultaneous crack tip and notch root propagation [Bao and Suo, 1992]. During this self-similar or steady state propagation, the bridging zone length remains constant (*i.e.*, the bridging zone propagates along with the crack). The two terms in  $J_{ff}$  (see Eq. 1 or 11) partition this total energy into notch root propagation and crack tip propagation. Clearly  $W_B(x_{root}) = J_{ff} - J_{tip}$  is the energy release rate for notch root propagation while the crack tip remains fixed; it evaluates only the energy in the increment of bridging zone that breaks done as the notch root advances. Finally, the remaining energy, or  $J_{tip} = J_{ff} - W_B(x_{root})$  must be the energy release rate for crack tip propagation while the notch root remains fixed. The two  $J$  integrals,  $J_{ff}$  and  $J_{tip}$ , are therefore sufficient for calculation of energy release rate for any combination of crack tip or notch root propagation.

## 2.1 Numerical Implementation

Traction-loaded cracks and numerical evaluation of  $J_{tip}$  and  $J_{ff}$  were implemented into the Material Point Method (MPM). MPM was selected because of its advantages for simulating crack propagation [Nairn, 2003] and the ease of including traction laws on explicit cracks; the details are in the appendix.

The evaluation of  $J$  integral by MPM for traction-free cracks is described elsewhere [Guo and Nairn, 2004]. Here the method was extended to account for crack tractions. Using Eqs. 9 and 10, evaluation of the two  $J$  integrals requires two paths — one inside and one outside the bridging zone. It is preferable to calculate both with a single path, which is easily achieved by use of Eq. 11:

$$J_{tip} = \begin{cases} J(x) - W_B(x) & x \leq x_{root} \\ J(x) - W_B(x_{root}) & x > x_{root} \end{cases} \quad (12)$$

and

$$J_{ff} = \begin{cases} J(x) - W_B(x) + W_B(x_{root}) & x \leq x_{root} \\ J(x) & x > x_{root} \end{cases} \quad (13)$$

Thus both  $J_{tip}$  and  $J_{ff}$  can be evaluated on the same arbitrary contour. With the exception of  $W_B(x_{root})$ , all calculations are local to the contour. The evaluation of  $J_{tip}$  when  $x > x_{root}$  or  $J_{ff}$  when  $x \leq x_{root}$  requires location of the notch root for evaluation of  $W_B(x_{root})$ . In MPM, a crack is defined by a linked list of massless particles; it is thus a simple task to scan along the crack to locate the notch root when needed.

Figure 3 shows calculation of  $J_{tip}$ ,  $J_{ff}$ , and  $J(x)$  by MPM as a function of the contour size. The calculation was for a single-edge notched specimen (SENT) of linear

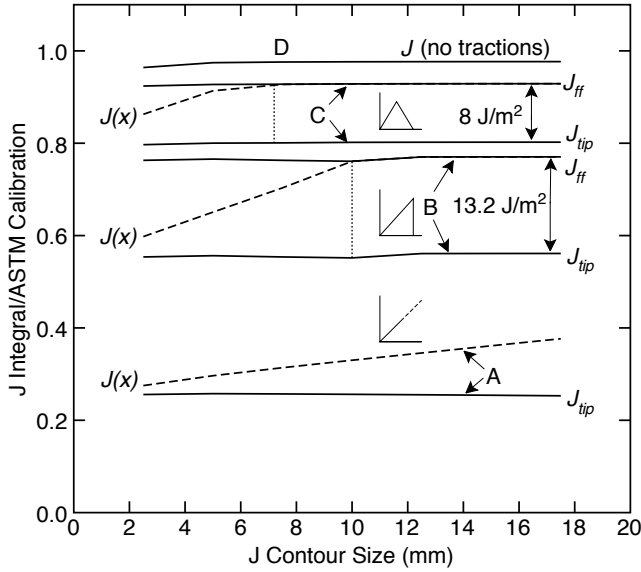


**Fig. 3** MPM Calculations of  $J_{tip}$ ,  $J_{ff}$ , and  $J(x)$  as a function of contour size for a single-edged notched specimen loaded in tension (200 mm  $\times$  50 mm with a 20 mm crack). A. Linear crack-tip tractions over the entire crack surface. B. Linear tractions over 10 mm of the 20 mm crack surface; the dotted vertical line is the end of the traction zone. C. A triangular traction law over 7.5 mm of the 20 mm crack surface; the dotted vertical line is the end of the traction zone. D. A crack with no crack-surface tractions.

elastic material ( $E = 70$  GPa,  $\nu = 0.33$ ) and dimensions 200 mm  $\times$  50 mm; the crack length was 20 mm and subjected to the various traction laws indicated in the figure. The  $J$  integral contour was chosen as a square centered on the crack tip [Guo and Nairn, 2004]; the  $x$  axis plots the distance from the crack tip to the contour or half the length of the square's sides. All results were normalized to the traction-free energy release rate for an SENT specimen [Williams, 1984]. Curves A are for a crack with a linear traction law over the entire crack surface.  $J_{tip}$  was independent of contour size while  $J(x)$  increased linearly. No calculation was done for  $J_{ff}$  because there is no notch root within the crack. Curves B show the same traction law, but only over half the crack surface. Both  $J_{tip}$  and  $J_{ff}$  were independent of the contour size.  $J(x)$  increased linearly while the contour was within the bridging zone and became identical to  $J_{ff}$  for contours outside the bridging zone. The difference between  $J_{ff}$  and  $J_{tip}$  (in absolute terms) was equal to  $W_B(x_{root})$  for the assumed traction law. Curves C show similar results for a triangular traction law over 7.5 mm of the 20 mm crack. The only difference was that  $J(x)$  increased non-linearly for contours within the bridging zone due to the non-linear traction law. Finally curve D is the single  $J$  integral for a crack with no tractions.

### 3 R Curve Analysis

The  $R$  curve is the actual energy released as a function of crack growth or of COD. It can be measured by experiments that directly measure energy released. Most experimental

methods, however, use indirect methods that involve calculation of  $R$  based on models for energy release rate. When these models are realistic, this approach gives the  $R$  curve, but if the models are unrealistic, the results should be labeled as an *effective*  $R$  curve or  $R_{eff}$ . For example, some work has associated  $J_{ff}$  with the  $R$  curve throughout the crack propagation process [Bao and Suo, 1992, Lindhagen and Berglund, 2000, Sorensen and Jacobsen, 2000]. Because  $J_{ff}$  is only valid when both the crack tip and the notch root are propagation, or during steady-state propagation, its use within the rising portion of the  $R$  curve, or during non-steady-state propagation, results in an  $R_{eff}$  curve.

Although  $R_{eff}$  is not the actual energy released, if it is defined consistently, it can be used to determine the traction law [Bao and Suo, 1992, Lindhagen and Berglund, 2000, Sorensen and Jacobsen, 2000]. For example, during crack propagation of a crack with opening displacements only, Eq. 11 leads to:

$$R_{eff} = J_{tip,c} + \int_0^{\delta_{root}} \sigma(\delta) d\delta \quad \text{and} \quad \sigma(\delta) = \frac{dR_{eff}}{d\delta_{root}} \quad (14)$$

where  $J_{tip,c}$  is the critical energy release rate for crack tip propagation, which is assumed to be a constant material property, and  $\delta_{root}$  is the notch root COD. The key experiment is to measure  $R_{eff}$  as a function of  $\delta_{root}$  and differentiate to find  $\sigma(\delta)$  [Lindhagen and Berglund, 2000, Sorensen and Jacobsen, 2000]. Unfortunately,  $R_{eff}$  normally cannot be determined from specimen loads and geometry because  $J_{ff}$  depends on the unknown traction law [Bao and Suo, 1992]. For a few specimens, however,  $J_{ff}$  is independent of the traction law, thus allowing measurement of  $R_{eff}$  [Bao and Suo, 1992]. One such specimen is a double cantilever beam (DCB) specimen with moment loads on the ends [Lindhagen and Berglund, 2000, Sorensen and Jacobsen, 2000]. Because  $R_{eff}$  can only be found in certain specimens, however, it cannot be used to confirm or deny whether traction laws are specimen-independent, material properties. One alternative is to switch to  $R$  rather than  $R_{eff}$ .

The  $R$  curve is a sum of the energy required to propagate the crack tip alone ( $J_{tip,c}$ ) and the energy released by the bridging zone itself:

$$R = J_{tip,c} + W_B(x_{root}) - W_B^{(r)}(x_{root}) = R_{eff} - W_B^{(r)}(x_{root}) \quad (15)$$

where the key new term is  $W_B^{(r)}(x_{root})$ , or the energy stored in the bridging zone that may be recovered upon unloading. Determination of the recoverable energy requires knowledge of the bridging zone mechanics. Figures 2C-F show commonly assumed traction laws with softening. Such laws cannot represent entirely elastic processes because that would imply an increasing load when unloading in the softening regime. The curves may, however, represent an elastic zone undergoing accumulation of damage such as by fiber breakage or fiber pull out when the zone is modeling fiber bridging. An elastic zone with damage will unload elastically to the origin; here, the unloading was assumed to be linear. The energy released from such a bridging zone becomes the shaded area in Fig. 4 and  $W_B^{(r)}(x_{root})$  is the area under the unloading curve.  $W_B^{(r)}(x_{root})$  decreases to zero for steady-state propagation, but may be non-zero during the rising  $R$  curve and is therefore essential to full analysis of  $R$  curves.

For crack propagation with opening displacements only and linear-elastic unloading, the  $R$  curve from Eq. 15 becomes

$$R = J_{tip,c} + \int_0^{\delta_{root}} \sigma(\delta) d\delta - \frac{1}{2}\sigma(\delta_{root})\delta_{root} \quad (16)$$

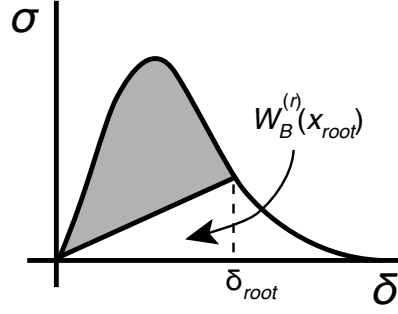


**Fig. 4** If the traction laws correspond to elastic processes with damage, the shaded area is the total energy released by the traction law and the area under the linear unloading line is the recoverable energy when loaded to  $\delta_{root}$ .

Differentiation yields

$$\frac{dR}{d\delta_{root}} = \frac{1}{2} (\sigma(\delta) - \delta\sigma'(\delta)) \quad (17)$$

Finally, this first-order differential equation for traction law can be solved to determine traction law from  $R'(\delta_{root})$  using

$$\sigma(\delta) = 2\delta \int_{\delta_{root}}^{\infty} \frac{R'(\delta)}{\delta^2} d\delta \quad (18)$$

This equation replaces Eq. 14 when  $R$  curve for actual energy released is measured instead of  $R_{eff}$ .

Two sample cohesive laws are a triangular law (see Fig. 2B):

$$\sigma(\delta) = \begin{cases} \sigma_c \frac{\delta}{\delta_{pk}} & \delta < \delta_{pk} \\ \sigma_c \frac{\delta_c - \delta}{\delta_c - \delta_{pk}} & \delta > \delta_{pk} \end{cases} \quad (19)$$

where  $\sigma_c$  is the maximum stress that occurs at  $\delta = \delta_{pk}$  and  $\delta_c$  is the failure COD, and a cubic law (see Fig. 2D [Hashemi et al, 1990, Needleman, 1987])

$$\sigma(\delta) = \frac{27\sigma_c}{4} \frac{\delta}{\delta_c} \left(1 - \frac{\delta}{\delta_c}\right)^2 \quad (20)$$

The cubic law has its peak at  $\delta = \delta_c/3$  and the nice property that  $\sigma'(\delta_c) = 0$ . Substitution of the triangular law into Eq. 15 gives

$$R(\delta) = \begin{cases} J_{tip,c} & \delta < \delta_{pk} \\ J_{tip,c} + J_B \frac{\delta - \delta_{pk}}{\delta_c - \delta_{pk}} & \delta_{pk} < \delta < \delta_c \end{cases} \quad (21)$$

where  $J_B = (1/2)\sigma_c\delta_c$  is the bridging zone toughness or area under the triangular traction law. For the cubic law

$$R(\delta) = J_{tip,c} + J_B \left(\frac{\delta}{\delta_c}\right)^3 \left(4 - 3\frac{\delta}{\delta_c}\right) \quad \text{for } 0 < \delta < \delta_c \quad (22)$$

where  $J_B = (9/16)\sigma_c\delta_c$  is the area under the cubic traction law.

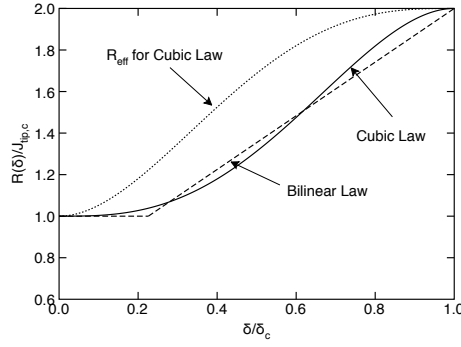


**Fig. 5** Theoretical rising portion of the  $R$  curves for triangular or cubic traction law and  $R_{eff}$  curve for cubic traction law in a normalized plot of  $R(\delta)/J_{tip,c}$  as a function of  $\delta/\delta_c$ . The bridging zone toughness was set equal to crack tip toughness,  $J_B = J_{tip,c}$ . The peak of the triangular law was chosen as  $0.2259\delta_c$ , which provides the closest possible match between  $W_B(x)$  for the two laws.

Normalized plots of  $R(\delta)$  for triangular and cubic laws assuming  $J_B = J_{tip,c}$  are in Fig. 5. The  $\delta_{pk}$  for the triangular law was set to  $0.2259\delta_c$ , which is the peak value that minimizes the least squares difference between  $W_B(x)$  for the two laws over the range  $0 < \delta(x) < \delta_c$ . The initial slow rise corresponds to predominantly elastic deformation in the bridging zone where most of the energy in the crack tractions is recoverable. The initial portion of the triangular law is perfectly flat because the deformation prior to  $\delta_{pk}$  is linear elastic. Once the bridging zone begins to release energy, the  $R$  curve rises more rapidly eventually reaching the steady state toughness as  $\delta \rightarrow \delta_c$ . For comparison, the dotted curve shows an  $R_{eff}$  curve for the cubic traction law derived from Eq. 14:

$$R_{eff}(\delta) = J_{tip,c} + J_B \left( \frac{\delta}{\delta_c} \right)^2 \left[ 6 - 8 \frac{\delta}{\delta_c} + 3 \left( \frac{\delta}{\delta_c} \right)^2 \right] \quad \text{for } 0 < \delta < \delta_c \quad (23)$$

$R(\delta)$  curves for bridging zones with elastic unloading are more sigmoidal than the corresponding  $R_{eff}(\delta)$  curves, which omit  $W_B^{(r)}(x_{root})$ . This issue is discussed in Sect. 5.

#### 4 Numerical Modeling of R Curves

The concepts of the previous section were implemented into Material Point Method (MPM) modeling [Nairn, 2007b]. MPM worked well because of its ability to model explicit cracks with crack propagation in arbitrary directions [Guo and Nairn, 2004, Nairn, 2003] and to incorporate history-dependent traction laws on all or part of the crack surfaces (see the Appendix). Numerical fracture modeling with bridging zones proceeded as follows:

1. An explicit crack was introduced into the MPM model by defining a series of connected crack particles.
2. At the start of the calculation, the one crack particle at the crack tip was assigned to a selected traction law with toughness  $J_B$ .
3. As the calculations proceed,  $J_{tip}$  was calculated. When  $J_{tip} \geq J_{tip,c}$ , where  $J_{tip,c}$  is the crack tip toughness, the crack tip was allowed to propagate. For the mode I

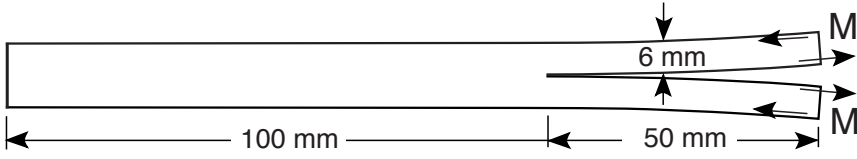


**Fig. 6** The geometry for the moment-loaded DCB specimen used the MPM fracture simulations. The moments were applied by equal and opposite forces applied to the top and bottom surfaces of the two arms.

cracks here, crack propagation was achieved by adding a new crack particle straight ahead of the crack tip. The length of the propagated crack segment was set equal to half the cell size of the background MPM grid. The new crack particle was assigned to the selected traction law with the COD initially equal to zero.

4. At the time of crack propagation, the actual energy released was calculated using Eq. 15.
5. On each time step, the COD on each crack particle was calculated and the notch root advanced whenever  $\delta_{root} \geq \delta_c$ .
6. The calculations continued until the crack length reached the end of the specimen.

This algorithm requires a numerical method that can calculate  $J_{tip}$ ,  $J_{ff}$ , and  $W_B^{(r)}$ ; this capability was demonstrated for MPM in Sect. 2. Notice, however, that crack propagation can be accomplished by use of  $J_{tip}$  alone. The only need for  $J_{ff}$  and  $W_B^{(r)}(x_{tip})$  is in the step for calculating the energy released. This output of the calculation plays no role in the crack growth mechanics, but is essential for modeling of  $R$  curves.

This modeling was applied to pure moment loading of a double cantilever beam (DCB) specimen (see Fig. 6). The specimen was 150 mm long, the arms were 6 mm thick, and the initial crack was 50 mm. The beam material was linear elastic with  $E = 2500$  MPa and  $\nu = 0.33$ . The crack tip toughness was  $J_{tip,c} = 100$  J/m<sup>2</sup>. The traction law was a cubic law with  $J_B = 100$  J/m<sup>2</sup> and the peak stress was varied among  $\sigma_c = 0.2$  MPa ( $\delta_c = 0.178$  mm),  $\sigma_c = 0.5$  MPa ( $\delta_c = 0.356$  mm), and  $\sigma_c = 1.0$  MPa ( $\delta_c = 0.889$  mm). The uniformly-spaced material points were separated by 0.25 mm. The pure moment loading was done by equal and opposite external forces applied to several material points on the top and bottom surfaces of each arm. To account for large displacements, the external forces rotated with the particles based on their rotational strains. The fully dynamic calculations increased the applied moment linearly with time. As previously noted, the moment-loaded DCB is a special specimen where  $J_{ff}$  (but neither  $J_{tip}$  nor  $W_B^{(r)}$ ) can be calculated without knowledge of the traction laws:

$$J_{ff} = \frac{12M^2}{b^2 E h^3} \quad (24)$$

where  $M$  is the applied moment and  $b$  and  $h$  are the width and thickness of the arms. The loading rate was selected such that  $J_{ff}$  reached  $J_{tip,c}$  in 10 ms. This rate approached quasi-static loading. During the loading phase, the total kinetic energy was less than 1% of the total energy in the specimen.

Figure 7 shows simulated  $R(\delta)$  curves where  $\delta$  is the COD at the location of the original notch root. The curves rose in a sigmoidal shape from  $J_{tip,c}$  to  $J_{tip,c} + J_B$  as  $\delta$  increased from 0 to  $\delta_c$ . The dashed lines are the theoretical  $R$  curves (see Eq. 22); they agreed well with the simulated  $R(\delta)$ , which validated the numerical model for

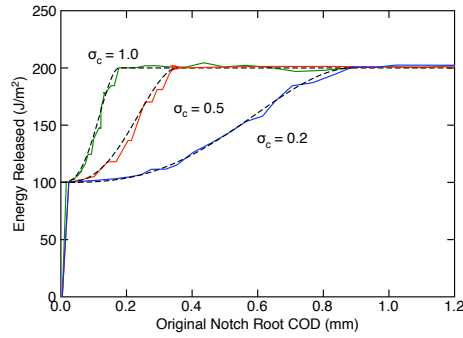


**Fig. 7**  $R(\delta)$  curves from fracture simulations of a moment-loaded DCB specimen for three different cubic traction laws that varied the peak stress,  $\sigma_c$ . The crack tip toughness was  $J_{tip,c} = 100 \text{ J/m}^2$ ; the bridging zone toughness was  $J_B = 100 \text{ J/m}^2$ . The dashed lines are theoretical predictions for the rising  $R$  curve for each assumed traction law (see Eq. 22).

crack propagation with bridging zones. The “noise” in the numerical results are a combination of spatial resolution (the cracks propagated in 0.25 mm jumps) and kinetic energy effects. The particle spacing was reduced until good results were obtained. A kinetic energy effect is inevitable in any dynamic crack propagation simulation. When a numerical model extends a crack, the system wants to release strain energy. In purely elastic calculations, all such released strain energy gets converted to kinetic energy. To control this non-physical build-up of kinetic energy, the calculations used global damping. Only a small amount of damping was used and it kept the total kinetic energy under 10% of the total energy. Calculations with no global damping confirmed that the damping used had no effect on the simulated  $R$  curves.

Experimental results more commonly record applied moment as a function of loading-point displacement or toughness as a function of crack growth (the traditional  $R$  curve). Numerical simulations for these results are in Fig. 8. For comparison, simulations with  $J_B = 0$  and  $J_{tip,c} = 100 \text{ J/m}^2$  or  $J_{tip,c} = 200 \text{ J/m}^2$  are plotted. These results reproduced the expected traditional fracture mechanics results of a horizontal and constant  $R$  curve; they show that the numerical crack propagation algorithm includes traditional fracture mechanics as a special case of bridging zone modeling by setting  $J_B = 0$ . The bridging zone simulations fell between the two fracture mechanics curves. They were near the lower limit when the cohesive stress was small and approached the upper limit as the cohesive stress increased. The simulated  $R$  curves are similar to the  $R(\delta)$  curves; *i.e.*, sigmoidal in shape. The relation between crack growth ( $\Delta a$ ) and COD ( $\delta$ ), however, depends on specimen geometry.

#### 4.1 Cohesive Zone Modeling

A cohesive zone, as originally proposed by Dugdale [1960] and Barenblatt [1962], is a crack-tip process zone where the tractions in the process zone exactly cancel the singularity at the crack tip. Cohesive zones are popular for crack propagation simulations in finite element analysis. Since the crack tip of a cohesive zone has no singularity, it does not advance by energy release rate, but rather by constitutive law of the material including line-zone mechanics. In essence, there is no crack tip. The material is instead

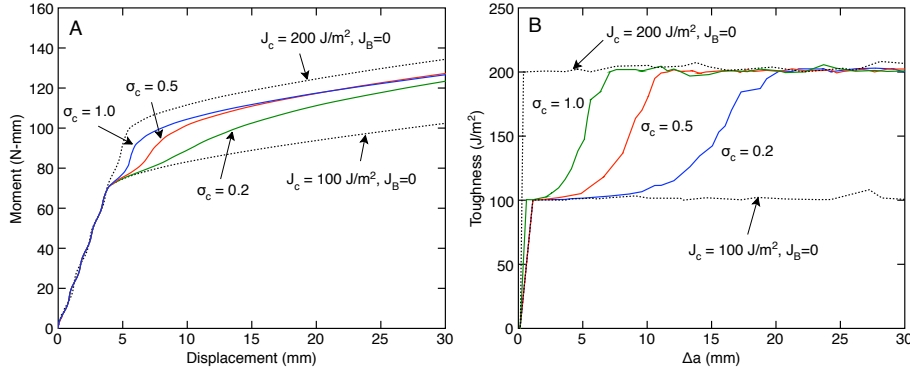


**Fig. 8** A. Moment-deflection results from fracture simulations of a moment-loaded DCB specimen. B.  $R(a)$  curves as a function of crack growth,  $\Delta a$ , for the same simulations. The simulations used three different cubic traction laws that varied the peak stress,  $\sigma_c$ . The crack tip toughness was  $J_{tip,c} = 100 \text{ J/m}^2$ ; the bridging zone toughness was  $J_B = 100 \text{ J/m}^2$ . The dotted lines are pure fracture mechanics simulations for toughness of  $J_c = 100 \text{ J/m}^2$  or  $200 \text{ J/m}^2$ .

modeled as a propagating process zone. The entire toughness is attributed to the process zone mechanics and the energy in the bridging law. The  $R$  curve modeling in this paper can provide a new type of cohesive zone by considering the special case where  $J_{tip,c} = 0$ . By this approach, the singularity at the crack tip is canceled and the entire toughness is due to the process zone. This new approach works for both elastic and inelastic process zones, since calculation of  $J_{tip}$  does not depend on recoverable energy in the process zone. All calculations here, however, are for  $R$  curves when the process zone is an elastic bridging zone.

Figure 9 shows simulated moment-deflection and  $R$  curves for the same DCB specimen simulated above but now for  $J_{tip,c} = 1 \text{ J/m}^2$  and  $J_B = 199 \text{ J/m}^2$ . The selection of  $J_{tip,c} = 1 \text{ J/m}^2$  rather than zero was to avoid numerical artifacts at the beginning of the calculation. If it was set to zero, the crack could propagate due to round-off error prior to any stress reaching the crack tip. Setting it to a finite value, however, held off crack propagation until the problem had sufficiently developed while still achieving the goal of effectively canceling the crack-tip singularity. Like the results in the previous section, the cohesive zone curves approached the fracture mechanics result as the cohesive stress increased. The moment-deflection curves approached it smoothly without the knee in the curves caused by crack tip processes. The  $R$  curves were sigmoidal from the beginning, rather than from  $J_{tip,c}$ , and were spread out over more crack growth (note the different scales for the  $x$  axes in Figs. 8B and 9B). The extra crack growth required to reach steady state crack propagation was a consequence of larger cohesive zone lengths compared to bridging zone lengths as shown in Fig. 10. Initially, both cohesive zones and bridging zones had zero length. They only started to develop when  $J_{tip}$  first reached  $J_{tip,c}$ . The cohesive zones started to develop immediately (the small offset was due to using  $J_{tip,c} = 1 \text{ J/m}^2$  instead of 0); the bridging zone started later. When each reached steady state, even for the same total toughness, the cohesive zone size was much larger. The cohesive zone lengths are a numerical solution to the Dugdale [1960] or Barenblatt [1962] problem of finding zone length as a function of applied load to cancel the singularity, but now for a specific finite-sized specimen and crack length.

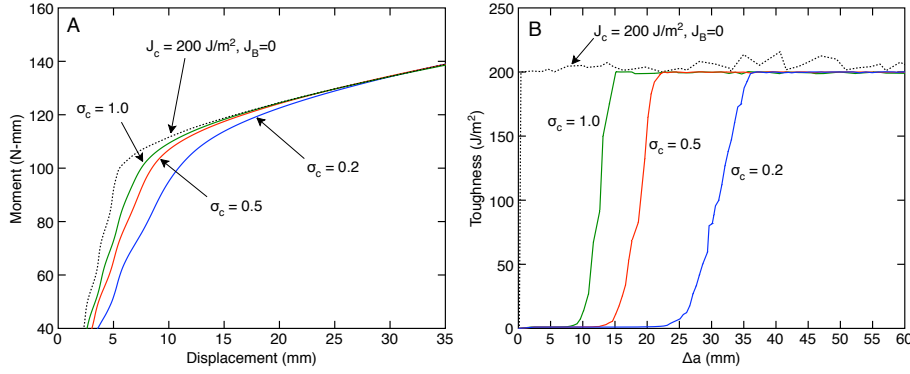


**Fig. 9** A. Moment-deflection results from fracture simulations of a moment-loaded DCB specimen with pure cohesive zones. B.  $R(a)$  curves as a function of crack growth,  $\Delta a$ , for the same simulations. The simulations used three different cubic traction laws that varied the peak stress,  $\sigma_c$ . The crack tip toughness was  $J_{tip,c} = 1 \text{ J/m}^2$ ; the bridging zone toughness was  $J_B = 199 \text{ J/m}^2$ . The dotted line is a pure fracture mechanics simulation for toughness of  $J_c = 200 \text{ J/m}^2$ .

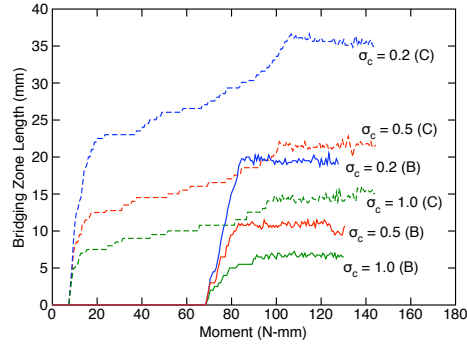


**Fig. 10** Bridging zone lengths as a function of applied moment for simulations with bridging zones, labeled “B,” or with pure cohesive zones, labeled “C,” each with three different cubic traction laws that varied the peak stress,  $\sigma_c$ . The bridging zone simulations had  $J_{tip,c} = J_B = 100 \text{ J/m}^2$ . The cohesive zone simulations had  $J_{tip,c} = 1 \text{ J/m}^2$  and  $J_B = 199 \text{ J/m}^2$ .

A problem in much cohesive zone modeling done by FEA is that the cohesive elements are introduced prior to the analysis. This approach requires the crack path to be known in advance. Because it eliminates the crack tip, finding the location of the actual crack tip is ambiguous (one must resort to *effective* crack length methods [Coureau et al, 2006]) and the entire fracture energy must come from the cohesive zone. Finally, because cohesive elements are unrealistically located in regions remote from cracks, the details of the traction law may cause numerical artifacts [de Borst et al, 2006]. In contrast, the MPM approach to cohesive zone modeling starts with no cohesive zone and allows it to develop naturally at the crack tip, possibly in arbitrary directions. This approach works for any crack path and unambiguously identifies the actual crack tip (which was needed when calculating  $R$  curves as a function of crack growth). Several FEA models have achieved similar results by adaptively inserting cohesive elements [de Borst et al, 2006, Pandolfi and Ortiz, 2002, Zhang et al, 2007].

These models relied on arbitrary element traction criteria for insertion of elements, rather than on dynamic elimination of the crack tip singularity. If the goal is a Dugdale [1960] or Barenblatt [1962] zone with no crack-tip singularity, the approach described here is preferable over traction criteria. A further advantage of having an actual crack tip and an ability to calculate  $J_{tip}$  is that the simulation can combine bridging zone processes with crack tip fracture mechanics (see previous section). This ability provides a more general approach.

## 5 Remarks on Experimental Methods

### 5.1 Measuring the $R$ Curve

The common fracture method of measuring load and crack length and calculating  $R$  through analysis cannot determine the  $R$  curve. Even if  $J_{ff}$  can be found (*e.g.*, moment-loaded DCB specimen), the  $R$  curve cannot be found because Eq. 15 depends on the traction law and on having enough physical insight into the bridging zone to be able to calculate the recoverable zone energy. If the process zone happens to have no recoverable energy, then  $R_{eff}$  and  $R$  will be same, but many process zones, such as fiber bridging zones, will have recoverable energy.

A viable alternative is to directly measure actual energy release rate. For example, the discrete area in Fig. 11A corresponds to the energy released as the crack grows. Dividing that area by the amount of crack growth that occurred gives the energy release rate [Hashemi et al, 1990]

$$R = \frac{1}{2B\Delta a}(F_1d_2 - F_2d_1) \quad (25)$$

where  $F_1$ ,  $F_2$ ,  $d_1$ , and  $d_2$  are the force and displacement before and after crack growth from  $a_1$  to  $a_2$ ,  $B$  is thickness, and  $\Delta a = a_2 - a_1$ . Unfortunately this approach is difficult because it requires subtraction of nearly equal values. A revised area method, illustrated in Fig. 11, has worked better in our recent experiments [Matsumoto and Nairn, 2008]:

1. Measure force and crack length as a function of load-point displacement.
2. Find the cumulative released energy per unit thickness by integrating the force,  $F(d)$ , up to displacement  $d$ , forming the function

$$U(d) = \frac{1}{B} \left( \int_0^d F(x) dx - \frac{d}{2}F(d) \right) \quad (26)$$

See shaded ‘‘Cumulative Area’’ in Fig. 11A.

3. By treating  $U(d)$  and  $a(d)$  as parametric functions of displacement, replot the cumulative energy as a function of crack length,  $U(a)$ . See the inset plot in Fig. 11B.
4. By energy analysis,  $R$  is the slope of  $U(a)$  or  $R = U'(a)$ . The slope calculation may benefit from smoothing by spline fits or running-regression methods.

The sample analysis in Fig. 11 is for published data for force and crack length in Hashemi et al [1990]. The solid line in Fig. 11C is the revised area method where the slope was found by least-squares, cubic spline fit to the  $U(a)$  curve in Fig. 11B. The open squares are calculation of  $R$  using the discrete area method in Eq. 25 [Hashemi et al,

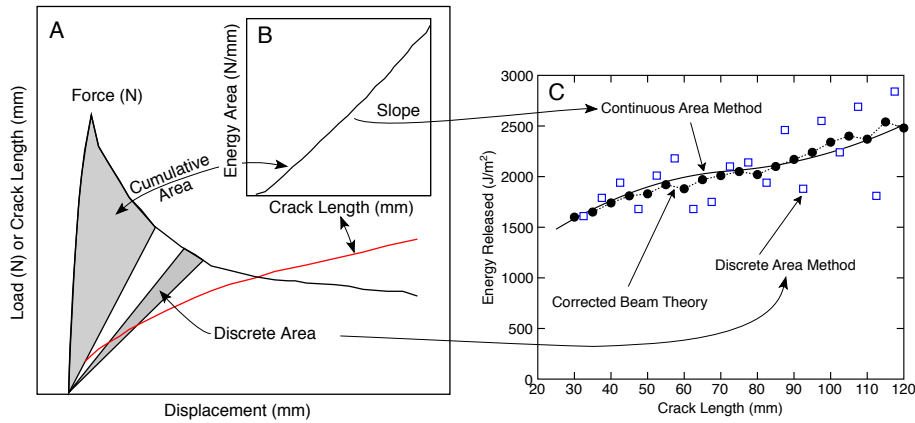


**Fig. 11** The area method for calculation of toughness. A. Experimental data for force and crack length as a function of displacement. The cumulative area is the total energy released up to some displacement. The discrete area is the energy released by a single increment in crack growth. B. The total energy released per unit thickness calculated from the cumulative area and then replotted *vs.* crack length. C. Calculation of  $R$  curve by slope of  $U(a)$  (smooth line), discrete area method (open squares), or corrected beam theory (filled circles). The latter two results are from Hashemi et al [1990].

1990]. The new area method significantly reduced the scatter. This new calculation also agreed well with the solid circles, which Hashemi et al [1990] claimed to be the most accurate results for energy release rate. The advantage of the new area method is likely related to elimination of the division by  $\Delta a$ .

## 5.2 Importance of Crack Tip *vs.* Notch Tip

Thus interpretation of rising  $R$  curves in terms of traction laws requires experimental determination of the actual crack tip and certainty that the notch root was not mistaken for the crack tip. All  $R$  curves in the previous section were plotted as a function of notch root COD or of crack length as measured from the actual crack tip. If the results were replotted as a function of crack length measured to the notch root, all  $R$  curves would converge to the ideal fracture mechanics result. The curves converge because the notch root remained fixed while the bridging zones developed and only propagated after reaching steady-state propagation and reaching a constant toughness.

The location of the crack tip is obvious in simulations, but may be uncertain in experiments. In some fiber-bridging zones, such as in unidirectional DCB specimens, crack tip identification can be done visually. In other specimens, such as medium density fiber board (MDF), the crack tip may be obscured [Matsumoto and Nairn, 2007]. One potential method for finding obscured crack tips is to use digital image correlation methods that can resolve full-field strain fields on the specimen surface [Bruck et al, 1989]. When the actual crack tip has a singularity, the full-strain field along the crack path will show a stress concentration at the crack tip [Matsumoto and Nairn, 2007]. If the bridged crack is a pure cohesive zone with no singularity this approach may not work, or conversely identification of a stress concentration in a bridging zone indicates that pure cohesive zone modeling of that fracture process will be unrealistic.

### 5.3 Interpretation of $R$ Curves

One use of  $R$  curves is to determine the traction law. Prior work [Lindhagen and Berglund, 2000] has used Eq. 14, but this method is only correct in experiments that measure  $R_{eff}$ . When experiments measure  $R$ , such as by the direct energy methods discussed above, the traction law must be found instead from Eq. 18. This new equation, however, assumes elastic unloading of the bridging law; alternative equations could be derived if different information is known about the recoverable energy in the bridging zone. It is a challenge obtaining fracture data that are sufficiently accurate for extracting the traction law. All possible  $R$  curves monotonically rise from  $J_{tip,c}$  to  $J_{tip,c} + J_B$  as  $\delta$  increases from 0 to  $\delta_c$ . A wide range of traction laws will make only minor differences in the  $R$  curve and thus experiments may be unable to differentiate those traction laws. Although the details of the traction law are a challenge, the global values are more accessible. The area under the traction law,  $J_B$ , is the difference between steady-state and initiation toughness. The critical COD,  $\delta_c$ , is given by the onset of steady-state crack growth in the  $R(\delta)$  curve. The maximum traction stress is given, within order unity, by  $\sigma_c \sim 2J_B/\delta_c$ .

In experiments that never reach steady state crack growth, one cannot measure either  $J_B$  or  $\delta_c$ . But, if one can infer the shape of the bridging law, it may be possible to measure  $\sigma_c$ . For example, Lindhagen and Berglund [2000] concluded that the bridging law for delamination approximates a linear softening law (see Fig. 2D). If the bridging law is linear softening, one can measure  $\sigma_c$  from the slope of  $R(\delta)$ , without needing to know  $J_B$  or  $\delta_c$ . Indeed, the delamination data in Fig. 11 is roughly linear with no evidence of reaching steady state. By estimating the notch root COD for experimental results to convert  $R(a)$  to  $R(\delta)$ , it was possible to estimate with  $\sigma_c \approx 0.06$  MPa (this calculation used beam theory with linear softening traction laws in Williams [2002]). A fiber-bridging interpretation  $R$  curve in Fig. 11 is thus fracture with  $J_{tip,c} \approx 1500$  J/m<sup>2</sup> and a linear softening zone with  $\sigma_c \approx 0.06$  MPa. This low cohesive stress contrasts with other attempts to model DCB delamination using cohesive zones (*e.g.*, [Blackman et al, 2003]). Cohesive zone modeling of DCB experiments requires high cohesive stress to get close to observed force-displacement curves. A high cohesive stress is simply allowing the cohesive zone model to approach a conventional fracture mechanics model; a physical interpretation of that stress “is not immediately obvious” [Blackman et al, 2003]. In contrast, a model with both crack-tip fracture and a bridging zone can simultaneously fit experimental force-displacement results while modeling the rising  $R$  curve using traction laws in the crack path. The experiments are explained better with a very low stress due to fiber bridging. This low stress leads to a non-negligible increase in toughness and has a clear physical interpretation.

### 5.4 $R$ Curve Shape

All  $R$  curves in this paper are sigmoidal in shape, but fracture mechanics texts [Atkins and Mai, 1988] and experimental results commonly show non-sigmoidal  $R$  curves that rise most rapidly in the beginning. This discrepancy may occur for several different reasons. First, the process zones here were assumed to correspond to elastic fracture phenomena that can retain some recoverable energy. If the process zone corresponds to a physical process with no recoverable energy, the  $R$  curve may rise more rapidly at the beginning. Second, the initial low slope in sigmoidal  $R$  curves can be associated with

elastic deformation in the traction law. If the law has no elastic regime (*e.g.*, a purely softening law), or the softening regime has a rapidly falling stress following by a long tail (*e.g.*, Fig. 2F as in [Coureau et al, 2006]), it is possible to get non-sigmoidal  $R$  curves. Third, observation of non-sigmoidal  $R$  curves may be a consequence of experiments measuring  $R_{eff}$  rather than  $R$ . For example, Lindhagen and Berglund [2000] observed non-sigmoidal  $R$  curves because they measured  $R_{eff}$ . Using their assumption of a linear softening law, the predicted  $R_{eff}$  can be derived from Eq. 14 to be:

$$R_{eff}(\delta) = J_{tip,c} + J_B \frac{\delta}{\delta_c} \left( 2 - \frac{\delta}{\delta_c} \right) \quad 0 < \delta < \delta_c \quad (27)$$

This non-sigmoidal shape agrees with the experimental results for  $R_{eff}$  in Lindhagen and Berglund [2000].

## 6 Conclusions

Most fracture models use *either* fracture mechanics criteria *or* cohesive zones in which the entire toughness comes from *either* crack-tip processes *or* a cohesive zone law. The methods here generalize fracture modeling to use *both* crack-tip fracture mechanics *and* fiber-bridging mechanics. By varying the ratio of  $J_{tip,c}$  to  $J_B$ , a family of models can be generated. As happens so often in science, whenever there are two extreme models, the best description of reality usually falls between the extremes. In fracture modeling, the two extremes are fracture mechanics and a pure cohesive zone. The best fracture modeling for many materials will likely be a combination of crack tip fracture mechanics and a bridging zone. The interpretation of the experiments will be toughness for crack tip processes and a toughness for the bridging zone processes.

Numerical implementation of crack propagation with a bridging zone requires a method that can calculate  $J_{tip}$ ,  $J_{ff}$ , and  $W_B^{(r)}$ . The method must also be able to handle both a bridging zone and an actual crack tip and to dynamically propagate the bridging zone from the crack tip based on  $J_{tip}$ . All these requirements are met by the MPM modeling used here, which makes it an effective tool for generalized fracture simulations. In contrast, prior cohesive zone methods that insert cohesive elements prior to the analysis are unacceptable because they do not have a crack tip. To implement similar modeling in FEA, the only need is for a package that is capable of calculating  $J_{tip}$  and of dynamically creating cohesive zone elements.

Modeling of  $R$  curves for any given traction law requires knowledge of both the traction law and of the recoverable energy in the process zone,  $W_B^{(r)}$ . This latter term requires physical interpretation of process zone mechanics in the form of assumptions about recoverable energy. All calculations here were based on traction laws representing elastic process and therefore with recoverable energy calculated by linear-elastic unloading. The extension to other types of process zones should be based on the actual mechanisms in the zone.

## Appendix: Bridging Zones in the Material Point Method

The material point method (MPM) was developed as a numerical method for solving problems in dynamic solid mechanics [Sulsky and Schreyer, 1996, Sulsky et al, 1994, 1995]. In MPM, a solid body is discretized into a collection of points much like a computer image is represented

by pixels. As the dynamic analysis proceeds, the solution is tracked on the material points by updating all required properties such as position, velocity, acceleration, stress state, *etc.*. At each time step, the particle information is extrapolated to a background grid that provides a platform for solving the equations of motion and updating all particle properties. The particles interact as a solid through the grid. Although MPM is frequently compared to finite element methods, a revised MPM derivation [Bardenhagen and Kober, 2004] presents it as a Petrov-Galerkin method that has more similarities with other meshless methods [Atluri and Shen, 2002]. The “meshless” nature of MPM derives from the fact that the body and the solution are described on the particles while the background grid is only used for calculations.

It is the meshless nature of MPM that recommends it for analysis of explicit cracks and here for extension to cracks with bridging zones. Although early MPM did not allow cracks (*i.e.*, did not allow displacement discontinuities), it has been extended to CRAMP, which signifies **CR**Acks in the **MA**terial **P**oint method [Guo and Nairn, 2004, 2006, Nairn, 2003]. The crack plane is defined by a linked series of massless particles that translate through the grid along with the material particles (see figures in [Nairn, 2003]). The crack particles track the local crack opening displacement that provides information for calculation of the top and bottom surfaces of cracks. Knowledge of the local stresses and the crack surfaces is sufficient for calculating fracture mechanics properties of crack tips such as  $J$  integral and stress intensity factors (Guo and Nairn 2004; 2006). Like the material points, the crack path is meshless and thus free to follow any arbitrary path.

Here, the CRAMP algorithm was extended to include traction laws. The main change was to search along each crack path on each time step and assign an external force to each crack particle within the bridging zone. The required force is found from the current crack opening displacement (COD). If the COD exceeds the critical COD, the traction zone is broken and thereafter exerts no force. Otherwise the traction is calculated and assigned to a force on the crack particle. Finally, the crack particle force is included in the the standard external force calculation task within the MPM algorithm [Nairn, 2003, Sulsky et al, 1994]. Two points require elaboration. First, normal tractions should be different in tension then in compression. This requirement was implemented within the CRAMP crack-contact algorithm [Nairn, 2003]. In brief, the crack was set to have frictionless contact [Bardenhagen et al, 2001], as described in [Nairn, 2003] and [Nairn, 2007a]. Whenever the crack was opened, the tractions were calculated using the traction law. Whenever the crack was in contact, the surfaces were prevented from cross over and the contact forces were calculated using the crack contact methods. For shear deformation, the traction laws were used for all tangential CODs; the frictionless nature of the crack contact eliminates all shear forces except those due to the shear traction law.

Second, since traction laws here are treated as describing elastic processes with damage, the softening region represents development of damage. Unloading within this region should not retrace the traction law, because that would result in an *increase* in traction. Here it was assumed that unloading returns linearly to the origin. This irreversibility was implemented by tracking the maximum COD reached on any crack particle. The resulting traction was then calculated as follows:

- The maximum displacement on each crack particle was initialized to  $\delta_{max} = 0$ .
- On each time step, if the current  $\delta > \delta_c$  then the traction law has failed and all tractions are removed from that crack particle; otherwise if  $\delta > \delta_{max}$  then  $\delta_{max} = \delta$ .
- Finally, the current  $\delta_{max}$  is used to find the traction force from

$$\sigma(\delta) = \frac{\sigma(\delta_{max})}{\delta_{max}} \delta$$

During monotonic loading, the traction follows the traction law. If unloading occurs at any crack particle, the tractions return linearly to the origin and remain on that line until  $\delta$  again reaches  $\delta_{max}$ . For shear tractions,  $\delta_{max}$  is the maximum of the absolute value of the tangential COD and shear deformations in either direction cause the same level of damage (*i.e.*, unloading remains on the same line through the origin until  $|\delta|$  again reaches  $\delta_{max}$ ).

Simulations that include crack propagation require calculation of  $J_{tip}$  followed by criteria for when and where to propagate the crack. The details are given in Section 4. Unlike FEA analysis of cracks, where cracks must follow mesh lines, a crack in CRAMP can proceed in arbitrary directions. Similarly, a bridging zone that follows behind the crack tip will follow those arbitrary directions. All calculations in this paper were done using the open-source, 2D CRAMP code [Nairn, 2007b].

---

## References

- Atkins AG, Mai YW (1988) *Elastic and Plastic Fracture Mechanics: Metals Polymers, Composites, Biological materials*. John Wiley & Sons, Ellis Horwood Limited, Chichester, West Sussex, England
- Atluri SN, Shen S (2002) The meshless local Petrov Galerkin (MLPG) method: A simple & less-costly alternative to the finite element and boundary element methods. *Computer Modeling in Engineering & Sciences* 3:11–52
- Bao G, Suo Z (1992) Remarks on crack-bridging concepts. *Appl Mech Rev* 45(6):355–366
- Bardenhagen SG, Kober EM (2004) The generalized interpolation material point method. *Computer Modeling in Engineering & Sciences* 5:477–496
- Bardenhagen SG, Guilkey JE, Roessig KM, Brackbill JU, Witzel WM, Foster JC (2001) An improved contact algorithm for the material point method and application to stress propagation in granular materials. *Computer Modeling in Engineering & Sciences* 2:509–522
- Barenblatt GI (1962) The mathematical theory of equilibrium cracks in brittle fracture. *Adv Appl Mech* 7:55–129
- Blackman BRK, Hadavinia H, Kinloch AJ, Williams JG (2003) The use of a cohesive zone model to study the fracture of fibre composites and adhesively bonded joints. *Int J Fract* 119:25–46
- de Borst R, Remmers JJC, Needleman A (2006) Mesh-independent discrete numerical representations of cohesive zone models. *Eng Fract Mech* 73:160–177
- Bruck HA, McNeill SR, Sutton MA, Peters WHI (1989) Digital image correlation using Newton-Raphson method of partial differential correction. *Experimental Mechanics* 28:261–267
- Coureau JL, Morel S, Gustafsson PJ, Lespine C (2006) Influence of the fracture softening behaviour of wood on load-COD curve and R-curve. *Materials and Structures* 40:97–106
- Dugdale DS (1960) Yielding of steel sheets containing slits. *J Mech Phys Solids* 8:100–104
- Guo Y, Nairn JA (2004) Calculation of J-integral and stress intensity factors using the material point method. *Computer Modeling in Engineering & Sciences* 6:295–308
- Guo Y, Nairn JA (2006) Three-dimensional dynamic fracture analysis in the material point method. *Computer Modeling in Engineering & Sciences* 16:141–156
- Hashemi S, Kinloch AJ, Williams JG (1990) The analysis of interlaminar fracture in uniaxial fibre reinforced polymer composites. *Proc R Soc Lond A347*:173–199
- Li VC, Chan CM, Leung CKY (1987) Experimental determination of the tension-softening relations for cementitious composites. *Cement and Concrete Research* 17:441–452
- Lindhagen JE, Berglund LA (2000) Application of bridging-law concepts to short-fibre composites part 1: DCB test procedures for bridging law and fracture energy. *Comp Sci & Tech* 60:871–883
- Matsumoto N, Nairn JA (2007) Fracture toughness of MDF and other materials with fiber bridging. In: *Proc. 22nd Ann. Tech. Conf. of the Amer. Soc. of Composites*, Seattle, Sept 17–19
- Matsumoto N, Nairn JA (2008) The fracture toughness of medium density fiberboard (MDF) including the effects of fiber bridging and crack-plane interference. *Eng Fract Mech* submitted
- Nairn JA (2003) Material point method calculations with explicit cracks. *Computer Modeling in Engineering & Sciences* 4:649–664
- Nairn JA (2007a) Numerical implementation of imperfect interfaces. *Computational Materials Science* 40:525–536
- Nairn JA (2007b) Source code and documentation for NairnMPM MPM software, <http://oregonstate.edu/~nairnj/>
- Needleman A (1987) A continuum model for void nucleation by inclusion debonding. *J Appl Mech* 54:525–531
- Pandolfi A, Ortiz M (2002) An efficient adaptive procedure for three-dimensional fragmentation simulations. *Engineering with Computers* 18:148–159
- Rice JR (1968) A path independent integral and the approximate analysis of strain concentration by notches and cracks. *J Applied Mech* June:379–386
- Smith I, Vasic S (2003) Fracture behaviour of softwood. *Mechanics of Materials* 35(8):803–815
- Sorensen BF, Jacobsen TK (2000) Large-scale bridging in composites: R-curves and bridging laws. *Composites Part A* 29:1443–1451

- Sulsky D, Schreyer HK (1996) Axisymmetric form of the material point method with applications to upsetting and Taylor impact problems. *Comput Methods Appl Mech Engrg* 139:409–429
- Sulsky D, Chen Z, Schreyer HL (1994) A particle method for history-dependent materials. *Comput Methods Appl Mech Engrg* 118:179–186
- Sulsky D, Zhou SJ, Schreyer HL (1995) Application of a particle-in-cell method to solid mechanics. *Comput Phys Commun* 87:236–252
- Williams JG (1984) *Fracture Mechanics of Polymers*. John Wiley & Sons, New York
- Williams JG (2002) Analytical solutions for cohesive zone models. *J Mech Phys Solids* 50:809–825
- Zhang Z, Paulino G, Celes W (2007) Extrinsic cohesive zone modeling of dynamic fracture and microbranching instability in brittle materials. *International Journal for Numerical Methods in Engineering* 72:893–923